A NOVEL FIELD CAGE DESIGN FOR THE CPS IPM AND SYSTEMATIC ERRORS IN BEAM SIZE AND EMITTANCE

K. Satou, KEK, Ibaraki-ken, Japan

J.W. Storey, S. Levasseur, G. Schneider, D. Bodart, CERN, Geneva, Switzerland

M. Sapinski, GSI, Darmstadt, Germany

Abstract

An ionization profile monitor has been recently installed in the CERN proton synchrotron. We present the design for a novel and simplified field cage structure that suppresses the secondary electrons that are induced by the ionized ions. We discuss the field cage design and the beam size and emittance systematic error considering the non-uniformity of the fields, the space-charge effect of the beam, and the lattice parameter errors.

INTRODUCTION

A new ionization profile monitor (IPM) has been developed and installed in the CERN proton-synchrotron (CPS) which includes a number of novel features, in particular: an electron imaging detector comprising multi-pixel silicon detectors that are bonded on Timepix3 readout chips [1]; a novel field cage to provide an electric field (E_c) to accelerate the ionized electrons onto the imaging detector that also suppresses the creation of background secondary electrons; a 3-pole self-compensating magnet to provide a 0.2 T magnetic field (B_g) to guide the electrons onto the imaging detector against a strong space charge electric field (E_s) and a novel 3-D particle-tracking code to simulate the profile to estimate the IPM-performance.

The new type of electron imaging detector has been previously reported [2, 3], and the general design of the IPM has also been reported [4]. The existing simulation codes that are used for an IPM are summarized in [5]. The first performance report of this IPM system was recently published [3], and the measured beam size was observed to be in good agreement (1% error) with the value that was measured using a wire-scanner monitor in the CPS.

The IPM was installed in the CPS at SS82 (s = 510−511 m) to measure the horizontal profile. The twiss-parameters at this location are $\beta_x = 12$ m, $\beta_y = 22$ m, and $D_x = 2.4$ m, $D_y = 0$ m. The horizontal and vertical beam size was calculated as follows:

$$\sigma_{x,y} = \sqrt{\frac{\varepsilon_{x,y}\beta_{x,y}}{\beta\gamma} + D_{x,y}^2\delta^2}, \sigma_l = D_x\delta, \delta = \frac{\Delta p}{p} \qquad (1)$$

The normalized emittance ε_x and ε_y is typically 1.5 and 1.6 μm, respectively. The contribution of a momentum dispersion (δ) to a beam size is dominant in case of an extraction beam. δ is typically 0.9E−3 for an injection beam and 1.5E−3 for an extraction beam. For an injection beam with the total kinetic energy (TKE) of 1.4 GeV ($\beta\gamma$ = 2.3), the horizontal size is 3.4 mm, which is 1.4 times larger than the beam size excluding the momentum dispersion. However, for an extraction beam with the TKE of 25 GeV ($\beta\gamma$ = 28), the beam size is 3.7 mm, which is

4.1 times larger. Consequently, the beam sizes at the injection and the extraction are observed to be similar. However, the vertical beam size decreases to 1/3.5 as $\beta\gamma$ increases.

FIELD CAGE DESIGN

The IPM field cage is depicted in Fig. 1, which is a simple structure that uses no side electrodes between the anode cathode that are generally used to improve the homogeneity of the field. The detector is mounted in a faraday cage to shield the detector system from beam induced RF interferences. The anode with a honeycomb-structured RF shield is placed above the detector and forms part of the faraday cage. The cathode is biased at a maximum voltage of −20 kV.

The IPM should only detect ionized electrons, which contain only about a hundred electrons per beam bunch [6]. The real signal is contaminated with: secondary electrons generated by the ionized ions that collide on the cathode; signals induced by primary and secondary beam losses; electrons from electron clouds and flash-over discharge. The second case can be avoided by precisely tuning the accelerator. If the latter two cases are observed to occur a significant number of electrons would be generated: some of these would be mixed into the real signals. Simulating such a situation requires detailed particle-tracking calculations for E_c and E_s. To reduce the secondary electrons that are generated by particle collisions, part of the cage structure is covered with titanium and carbon coating.

The cathode contains an ion trap to reduce the secondary electrons generated by the ion collisions; the ion trap structure is described in the following section.
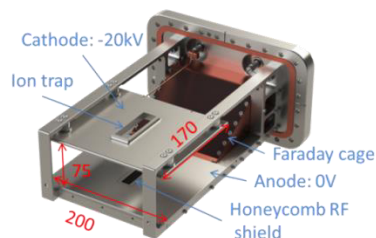

Figure 1: Field cage of the CPS IPM.

Noble Ion-Trap Structure

Secondary electrons are generated when ions collide with the cathode. These electrons are then reaccelerated to the anode and the detector where these signals are mixed with the real signals. The position distortion of ions due to the E_s on the cathode is larger than that of the ionized electrons on the anode. This difference is due to the gyra-

tion motion with B_g. Since the Larmor radius is a linear function of the ionic masses, the radius of ions is 1,800 times greater than the radius of an electron. Therefore, mixed signals exhibit the following two components: a real beam profile and a broad-structured distribution that is observed to originate from the ion-induced secondary electrons.

To repel the secondary electrons from the cathode a grid mesh is typically placed in front of the cathode, and a gap voltage is applied between the grid and the cathode. However, this method cannot eliminate the secondary electrons generated at the grid wire caused by the ion-bombardment process (as shown in Fig. 2).
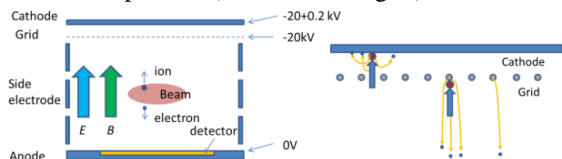

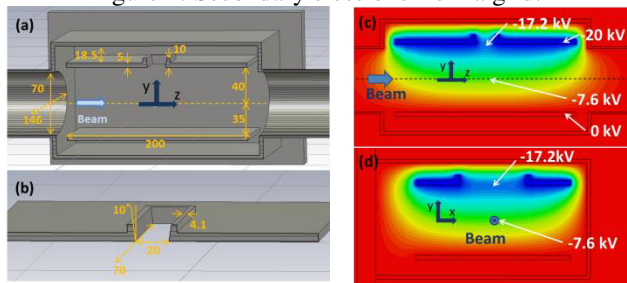Figure 2: Secondary electrons from a grid.

Figure 3: The field cage with an ion-trap structure and its potential map.

To completely eliminate the signals of secondary electrons, an ion-trap was primarily designed for this IPM (Fig. 3). A window on the cathode acts as an ion trap. The window is placed just above the detector and is 70 × 20 mm^2 in size, which is larger than the active area of the detector (56.9 × 14.0 mm^2). The inside wall of the window was cut diagonally by 10 degrees. An electric field inside the window pushes the secondary electrons that are generated on the surface of the inside wall in an upward direction. Because the window distorts the E_c, the cathode is shifted in an upward direction by 5 mm from the symmetrical position of the anode to avoid undesirable fields near the window (Fig. 3). Figure 3 also shows the potential in the chamber calculated using the CST software suite [7].

The operating principle of the ion-trap is as follows.

1. The ions pass through the ion-trap window.
2. The ions are decelerated by the electric field between the cathode and the chamber wall, stop between them, and are then accelerated again onto the backside of the cathode.
3. The ions hitting the backside of the cathode generate secondary electrons. These electrons are accelerated toward the chamber wall and collide with it; however, the emission of secondary electrons is terminated in this case since the chamber is the anode.

A CST particle-tracking simulator was used to simulate ionic motion. Figure 4-(a) depicts the trajectory of ions

emitted from a virtual emission plate positioned at the beam axis. The dimension of the plate is set to be equal to the size of the detector. Almost all the ions are observed to collide with the backside of the cathode or the inside wall of the ion-trap window. In this calculation, only three particles out of 70 are observed to return to the inside surface of the cathode. However, the generated secondary electrons that originate from these ions cannot reach the detector. Figure 4-(b) depicts the trajectories of the secondary electrons generated at the inside wall of the ion trap emitted with the TKE of 10 eV. The emitted electrons return to a point near the emission point by a gyrating motion with the B_g of 0.2 T with the radius of about 50 μm, and some of the emitted electrons are accelerated to the chamber wall and collide with it.
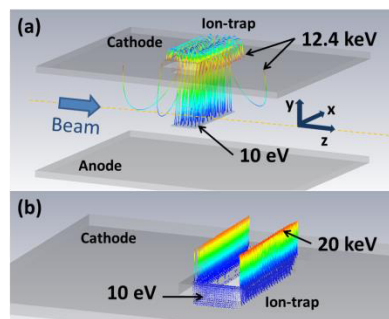

Figure 4: Particle trajectory calculations. (a) Ions to the ion-trap and (b) secondary electrons from the inside wall of the ion-trap accelerated to the chamber wall.

SYSTEMATIC ERROR OF BEAM SIZE

The influence of field distortion on the measured beam size was monitored using the 3D-particle-tracking code, IPMsim3D [5, 8], which was developed for this project. Details of the code will be published in a forthcoming publication. This code uses 3D fields of the E_c and B_g that were estimated using an external code, whereas E_s was estimated internally. E_c was calculated using CST Studio. B_g was assumed to have a uniform distribution of 0.2 T. A point-spread function (PSF) was calculated analogously to the optical design. The electron source that is defined in this study is not a point but a line with a length of $\Delta z = 14$ mm, which covers the longitudinal extent of the detector. The trajectory of electrons emitted at different positions on the line was estimated.

One standard deviation on a histogram of electrons that were hitting the detector is chosen to be the measure of point spread. An E_z field along the z axis creates point spread because the $E_z \times B_g$ drift makes a horizontal-position shift. By varying the line position, a 2D map of the PSF was obtained. Similar calculations were conducted using CST. These results were observed to be consistent (Fig. 5). Figure 5 shows the point spread at different positions of y when x = 0; it also depicts that the point spread near the anode is less than 1 μm. In contrast, the point spread becomes larger from y = 9 mm as it approaches to the window. At 10 mm there is a local minimum of approximately 1 μm, which is smaller than the value that is calculated for the case of no window. The E_z

vectors originated from the cathode edge (at $z = \pm$ 100 mm) and from the window exhibit opposite directions; moreover these fields are offset at this point.

In the main region of interest ($-15 < x < 15$ mm and $-15 < y < 15$ mm) the point spread is less than 10 μm. Assuming the PSF to be a Gaussian function and a constant PSF value of 10 μm, the systematic error on the beam size is estimated to be approximately 6E-4%.

The PSF from other error sources, including: the non-uniformity of B_g, the initial momentum of the ionized electrons, and E_s were also checked using the code. The magnet is designed to ensure that B_x and B_z remained less than the order of $O(-3)$ of B_y. The $B_{x,z}$ were assumed to have a linear function of z, which is $B_{x,z} = \frac{10^{-3}B_y}{7mm}z$ within the longitudinal extent of the detector. The initial momentum of the electrons was calculated assuming that the residual gas in the IPM is pure hydrogen gas. The code calculates the double-differential cross section and estimates the initial momentum of electrons obtained by the ionization. The PSFs are also depicted in Fig. 5 for these additional error sources. The estimated total PSF, including all error sources, was approximately 30 μm. The effect of this PSF is a 3E-3% systematic error of the beam size measurements.
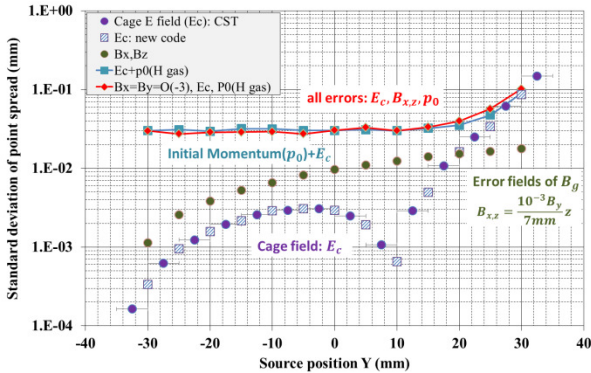

Figure 5: PSFs regarding the E_c and B_g fields, and the initial momentum of the detached electrons

The profile distortion due to E_s was previously reported in [4]. The systematic error on the measured beam size is 3E-2% when B_g is 0.2 T. The error is less than the required error of 0.5%. There is an error originating from the pixel size of the detector, which is 55 μm. The spatial resolution is thus 55/sqrt(12) μm and the resulting systematic error is approximately 9.2E-4%.

SYSTEMATIC ERROR OF EMITTANCE

The systematic error for emittance that is discussed in this study is in a similar manner as that in [9, 10]. The required systematic error is 10% [11]. The horizontal beam emittance can be calculated using the slip factor, η, as in Eq. (2), where T_s is the revolution period of the synchronized particle and σ_t is the longitudinal beam size. The factor A is defined as $A = D_x/\eta$. The error components on each factor are exhibited in Eq. (3). The values for σ_x and δ are assumed to be as 3.6 mm and 0.9E-3 for injection and 3.7 mm and 1.5E-3 for extraction. The con-

tributions of longitudinal motions dominate for the extraction beam. The error is 10 to 30 times greater than that observed in the injection beam because there is only a singular point at which a beam satisfies the condition $\sigma_x = \sigma_l$. Each systematic error is summarized in Table 1.

$$\varepsilon = \frac{\beta\gamma}{\beta_x}\left(\sigma_x^2 - \left(\frac{D_x}{\eta}\frac{\sigma_t}{T_s}\right)^2\right) = \frac{\beta\gamma}{\beta_x}\left(\sigma_x^2 - A^2\left(\frac{\sigma_t}{T_s}\right)^2\right) \quad (2)$$

$$\frac{\Delta\varepsilon}{\varepsilon}\bigg|_{\beta_x} = -\frac{\Delta\beta_x}{\beta_x}$$

$$\frac{\Delta\varepsilon}{\varepsilon}\bigg|_{\sigma_x} = \frac{2\sigma_x^2}{\sigma_x^2 - \sigma_l^2}\frac{\Delta\sigma_x}{\sigma_x} = 3.1\frac{\Delta\sigma_x}{\sigma_x} \text{ for inj.}, 37.5\frac{\Delta\sigma_x}{\sigma_x} \text{ for ext.}$$

$$\frac{\Delta\varepsilon}{\varepsilon}\bigg|_A = \frac{-2\sigma_l^2}{\sigma_x^2 - \sigma_l^2}\frac{\Delta A}{A} = -1.1\frac{\Delta A}{A} \text{ for inj.}, -35.5\frac{\Delta A}{A} \text{ for ext.} \quad (3)$$

$$\frac{\Delta\varepsilon}{\varepsilon}\bigg|_{\sigma_t} = \frac{-2\sigma_l^2}{\sigma_x^2 - \sigma_l^2}\frac{\Delta\sigma_t}{\sigma_t} = -1.1\frac{\Delta\sigma_t}{\sigma_t} \text{ for inj.}, -35.5\frac{\Delta\sigma_t}{\sigma_t} \text{ for ext.}$$

$$\frac{\Delta\eta}{\eta} = -2\frac{1}{\eta}\left(\gamma_T^{-2}\frac{\Delta\gamma_T}{\gamma_T} + \gamma^{-2}\frac{\Delta\gamma}{\gamma}\right) \quad (4)$$

Table 1: Summary of Systematic Errors

	Value	Error(systematic)
β_x	12 m	1%
D_x	2.4 m	1% (assumed)
σ_x	3.6/3.7 mm	3E-2%(estimated)
$\beta\gamma$	2.28/27.6	0%
γ_t	6.01	±0.005
η	0.134/0.026	0.034%/0.18%
$A=D_x/\eta$	17.9/92.3 m	1.0%/1.2%
σ_t	45/0.75 ns	4E-5%/1.4E-1%

The systematic error on β_x and γ were set to 1% and 0%, respectively, as depicted in [9]. The systematic error for D_x was assumed to be 1% similar to that of β_x. The error on the phase slip factor, η, can be expressed using Eq. (4). The relativistic Lorenz factor at the transition energy, γ_T, was observed to be 6.01 ± 0.005 [12]. The systematic errors of the slip factor were further observed to be 0.034% and 0.18%, and the errors of factor, A, for injection and extraction beam were 1.0% and 1.2%, respectively. During longitudinal profile measurement, the system yields a beam width of $\sqrt{\sigma_T^2 + \Delta t^2}$ if the measurement system exhibits a time resolution of Δt, which is a Gaussian-function-type response. The step response of the wall current monitor for the CPS [13] is 206 ps for a 10-90% rise time; thus, it is reasonable to consider 40 ps to be the value of Δt.

The simple sum of these absolute values is observed to limit the systematic error. The estimated statistical error for the injection beam is 2.2%; however, it is observed to be approximately 50% for the extraction beam. The main contribution for the extraction beam is sourced from factor A.

SUMMARY

A novel ion-trap structure was developed for the ionization profile monitor (IPM) for the CERN proton synchrotron to eliminate the secondary electrons that are otherwise formed by the collision of ions on the cathode or grid-wires. The field non-uniformity of the field cage was calculated, and the point-spread function was obtained. The expected systematic error for the beam size is 3E-3%, whereas the errors for emittance are 2.2% for the injection beam and 50% for the extraction beams.

REFERENCES

[1] T. Poikela *et al.*, "Timepix3: a 65K channel hybrid pixel readout chip with simultaneous ToA/ToT and sparse readout", 2014 *JINST* 9 C05013.

[2] S. Levasseur *et al.*, "Development of a rest gas ionization profile monitor for the CERN proton synchrotron based on a Timepix3 pixel detector", in *Proc. TWEPP2016*, Karlsruhe, Germany.

[3] J.W. Storey *et al.*, "First results from the operation of a rest gas ionization profile monitor based on a hybrid pixel detector", in *Proc. IBIC2017*, Grand Rapids, MI, USA, 2017, WE2AB5.

[4] J.W. Storey *et al.*, "Development of an ionization profile monitor based on a pixel detector for the CERN proton synchrotron", in *Proc. IBIC2015*, Melbourne, Australia, 2015, pp. 470-473.

[5] M. Sapinski et al., "Ionization profile monitor simulations – status and future plans", in *Proc. IBIC2016*, Barcelona, Spain, 2017, pp. 520-523.

[6] M. Sapinski *et al.*, "Feasibility study of BGI monitor for PS", Oct, 29, 2014, EDMS 1396633.

[7] CST-Computer Simulation Technology, http://www.cst.com/

[8] IPMsim, http://twiki.cern.ch/twiki/bin/view/IPMsim/

[9] G. Sterbini *et al.*, "Beam-based measurement of the CPS wire scanner precision and accuracy", in *Proc. IPAC2014*, Dresden, Germany, 2014, pp. 3674-3676.

[10] G. Sterbini *et al.*, "Emittance characterisation of high brightness beams in the CERN PS", in *Proc. IPAC2016*, Busan, Korea, 2016, pp. 299-302.

[11] E.B. Holzer *et al.*, "Functional specifications for beam transverse profile measurement as part of the LHC injectors upgrade and consolidation projects", EDMS1233010 v.1, 2018.

[12] R. Cappi, J.P. Delahaye, K.H. Reich, "PS beam measurement at flat-top fields near transition energy", *IEEE Trans. Nucl. Sci.*, Vol. NS-28, No. 3, (1981) 2389.

[13] J. Durand, "Combining wideband signals from a wall current monitor", *PS/LP/Note,* 94-14(Tech.).